Arabian Journal of Chemistry (2022) **15**, 103498

King Saud University

Arabian Journal of Chemistry

www.ksu.edu.sa
www.sciencedirect.com

ORIGINAL ARTICLE

Two new Cd(II)/Co(II) compounds: Luminescent and photocatalytic property, and treatment activity on coronary artery atherosclerosis

Hai-Bo Yu [a,b,1], Feng-Jiang Chen [c,1], Jing Li [d], Yu-Ming Kang [a,*], Yun-Kun Zhang [e], Yuan Shan [e]

[a] *Department of Physiology and Pathophysiology, Xi'an Jiaotong University School of Basic Medical Sciences, Key Laboratory of Environment and Genes Related to Diseases of Education Ministry of China, Xi'an 710061, China*
[b] *Department of Cardiovascular Medicine, Jiamusi University First Affiliated Hospital, Jiamusi 154002, China*
[c] *Department of Physiology, Heilongjiang University of Chinese Medicine, Jiamusi College, Jiamusi 154002, China*
[d] *Department of Physiology, Jiamusi University Basic Medical College, Jiamusi 154007, China*
[e] *Department of Medicine, Hebei University, Shijiazhuang 071002, China*

Received 26 July 2021; accepted 11 October 2021
Available online 18 October 2021

KEYWORDS

Luminescence;
Photocatalysis;
Coronary artery atherosclerosis

Abstract Two new compounds, namely $[Cd_2(L)_2(4\text{-pybim})_2(H_2O)]_n\cdot 3n(H_2O)$ (**1**) and $[Co(cam)(4\text{-pybim})_2(H_2O)]$ (**2**) (H_2L = succinic acid, H_2cam = D-(+)-camphoric acid, 4-pybim = (4-pyridyl)benzimidazole), were successfully synthesized by the combination of carboxylate ligand, 4-pybim ligand and corresponding metal salts. Moreover, the luminescent property of **1** and photocatalytic activity of **2** were also investigated in detail. The application values of the new compounds against coronary artery atherosclerosis were evaluated and the detail mechanism was assessed simultaneously. First of all, the inflammatory cytokines levels released into plasma after compound treatment was measured with the detection of enzyme-linked immunosorbent assay. Then, the relative expression of the signaling pathway of NF-κb in the vascular endothelial cells was tested through exploiting the real time reverse transcription-polymerase.

1. Introduction

According to WHO statistics, in 2015, cardiovascular diseases, dominated by coronary and cerebrovascular atherosclerosis, caused nearly 15 million deaths worldwide, accounting for more than 25% of all deaths (Libby and Theroux, 2005). Due to various reasons, the prevalence of atherosclerosis in developing countries is still increasing, and due to the pro-

* Corresponding author.
E-mail address: yumingkang66@163.com (Y.-M. Kang).
[1] Authors are contributed equally to this work.
Peer review under responsibility of King Saud University.

Production and hosting by Elsevier

https://doi.org/10.1016/j.arabjc.2021.103498
1878-5352 © 2021 The Authors. Published by Elsevier B.V. on behalf of King Saud University.

longed life span of the population, the incidence is also increasing (Boudoulas et al., 2016).

Metal-organic frameworks (MOFs), to date, has been considered to be one type of superior hybrid functional materials employed in molecular recognizer, luminescence sensing, gas separation and gas storage, non-linear optics, magnetism and other areas, owing to their large surface area and porosity, tunable pore structure, high thermal/chemical stability, diversified topological architectures (Fan et al., 2021; Wang et al., 2021; Zhao et al., 2021; Fan et al., 2022; Hu et al., 2020). In order to obtain the MOFs, it is important for us to choose an appropriate multifunctional organic building block and central metal ion with specific coordination geometry. The coordination-driven self-assembly process is very subtle that can be affected through a variety of unpredictable factors, for example, the temperature of reaction, pH, solvent, structure-directing agent, the ratio of ligand and metal, together with auxiliary ligand (Xue et al., 2018; Hu et al., 2018; He et al., 2018; Dutta et al., 2021). Therefore, achieving controllable syntheses of MOFs at molecular level remains a huge challenge to chemists. As an effective synthetic strategy, mixed-ligand self-assembly strategy that usually combine two function-different ligands, such as carboxylate ligand and N-donor ligand, has been widely used to construct MOFs with desired structures and application properties owing to the synergistic bridging effect of the function-different ligands, which not only combine the characteristics of two function-different ligands into one MOF but also achieve better performance and structural diversity of MOFs (Liu et al., 2021; Singh et al., 2021; Qin et al., 2020; Wen et al., 2016; Wu et al., 2017; [illegible] et al., 2020).

As a N-donor ligand, (4-pyridyl)benzimidazole (4-pybim) with a large π-electron conjugated group, has three coordination sites, and may coordinate metal ions into novel MOFs that can serve as good photoactive materials attributed to the large π-electron conjugated group. By [illegible] the organic carboxylate ligand, Yao and his-co-workers employing (n-pyridyl)benzimidazole (n = 2, 3, 4) as reported a sequence of Zn(II)/Cd(II) MOFs exhibiting different structures and excellent luminescent properties (Pan et al., 2020; Banerjee et al., 2014). On the other hand, among various ligands available, amino acids, benzimidazoles and polypyridyl ligands (1,10-phenanthroline, bipyridine, etc.) were chosen owing to their advantageous properties. Benzimidazole derivatives interact easily with biomolecules of living systems, due to their structural relevance with naturally occurring nucleotides. Hence, they have been extensively utilized in drug design and medicinal chemistry. Furthermore, the benzimidazole derivatives serve as good ligands for transition metal ions due to the large conjugated π-system and the azomethine nitrogen. The introduction of additional substituent on the benzimidazole nucleus could potentially affect the interaction of the molecules with biological targets. Hence, a wide variety of benzimidazole-based metal complexes were found to be efficient catalytic and biologically active compounds (Sabithakala and Chittireddy, 2018; Cassemiro et al., 2020). Considering that, in this work, we selected (4-pyridyl) benzimidazole along with two diverse dicarboxylic acid ligands (succinic acid and D-(+)-camphoric acid) to separately react with Cd(II) and Co(II) ions under the conditions of hydrothermal, obtained two novel coordination compounds triumphantly, i.e., $[Cd_2(L)_2(4\text{-pybim})_2(H_2O)]_n\cdot 3n(H_2O)$ (1) and $[Co(cam)(4\text{-pybim})]_n\cdot n(H_2O)$ (**2**) (H_2L = succinic acid, H_2cam = D-(+)-camphoric acid, 4-pybim = (4-pyridyl) benzimidazole). The luminescent property of **1** and photocatalytic activity of **2** were also investigated. The sequence of bio-activities were implemented and the novel compounds' mechanism were discussed as well.

2. Experimental

2.1. Materials and instrumentation

From Jinan Henghua company, we can gain the raw reagents, which could be directly used. In order to investigate the elements of Carbon, Nitrogen together with Hydrogen, Vario EL III was employed. Through applying PANalytical X'Pert Pro, the pattern of PXRD could be analyzed at 0.05° step size through applying the Cu/Kα radiation (in which λ is 1.54056 Å). From 30 to 800 ℃ temperature, TGA was accomplished with the NETZSCHZ STA-449C at 10 ℃ per min heating rate under flow of nitrogen. Edinburg FLS920 TCSPC was utilized to test the luminescence spectra in solid state at environmental temperature.

2.2. Synthesis of $[Cd_2(L)_2(4\text{-pybim})_2(H_2O)_2]_n\cdot 3n(H_2O)$ (1) and $[Co(cam)(4\text{-pybim})]_n\cdot n(H_2O)$ (2)

A mixture generated by 0.2 of mmol H_2L, 0.2 mmol $Cd(Ac)_2\cdot 2H_2O$, 0.2 mmol of $NaHCO_3$, 0.2 mmol 4-pybim, 10 mL H_2O was stored into the Teflon-lined stainless steel (23 mL) and it then in-depth heated under 160℃ temperature for three days. The **1**'s colorless massive crystals were generated after cooling the above product to the environmental temperature with 2 ℃/min cooling rate and the yield of the crystal is 32% in accordance with the $Cd(Ac)_2\cdot 2H_2O$. Anal. Calcd. (%) for the $C_{32}H_{36}Cd_2N_6O_{13}$ (937.49): N, 8.96, C, 40.96 and H, 3.84. Found (%): N, 8.95, C, 40.98 and H, 3.81. IR (KBr, cm^{-1}, Fig S1): 3462 w, 3124 w, 2938 w, 1555 s, 1507 w, 1407 s, 1325 w, 1288 s, 1145 m, 1075 m, 1002 w, 934 w, 881 w, 741 m, 670 w.

The mixture synthesized from 0.2 mmol $Co(Ac)_2\cdot 4H_2O$, 0.2 mmol H_2cam, 0.2 mmol of 4-pybim, 10 mL H_2O and 0.2 mmol of $NaHCO_3$, was sealed into the Teflon-lined stainless steel (23 mL) and it was subsequently in-depth heated under 160℃ temperature for 72 h. The **2**'s purple massive crystals were formed after cooling the above mixture to ambient temperature with 2℃/min cooling rate and the yield of the crystal is 41% on the basis of $Co(Ac)_2\cdot 4H_2O$. Anal. calcd. (%) for $C_{22}H_{24}CoN_3O_5$ (469.37): N, 8.95, C, 56.25 and H, 5.11. Found (%): N, 8.97, C, 56.22 and H, 5.08. IR(KBr pallet, cm^{-1}): 3403 w, 3114 w, 2931 w, 1552 s, 1506 w, 1403 m, 1342 w, 1289 m, 1147 m, 1000 w, 771 w, 670 w.

2.3. X-ray crystallography

For the two compounds, their data of single crystal were recorded with the Mercury CCD, which was equipped with the graphite monochromated Mo–Kα radiation (where λ is 0.71073 Å) under ambient temperature. *ShelxT* with dual direct method and *SHELXL*-2014 with full-matrix least square technology in accordance with F^2 were respectively employed

to solve and refine the compounds' architectures (Sheldrick, 2015). All of the non-H atoms were anisotropically refined. The complexes' architectural optimization along with their data of crystallography are illustrated in the Table 1. And Table S1 reflects the chose angles (°) along with lengths (Å) of bond for the compounds.

2.4. Photocatalytic experiment

50 mg powders of **1** were added to the aqueous solution of methyl violet (MV) (100 mL, 10 mg·L^{-1}). After that, the suspension was maintained for one hour in darkness to establish the absorption–desorption equilibrium (Fig S4). After that, the as-prepared mixture was exposed to the lamp irradiation with 125 W Hg (365 nm, Beijing Zhongjiao Jinyuan). Then, 5 mL reaction solution was taken out every 15 min, and further centrifugally separated to remove the trace amounts of powders. The obtained solution was finally analyzed by the UV–Vis spectrophotometer.

2.5. Enzyme linked immunosorbent assay (ELISA)

To determine TNF-α content and IL-18 content released via vascular endothelial cells into the plasma after treated by the complex, the enzyme-linked immunosorbent assay detection was applied in our experiment. This study was carried out strictly following the instructions's guidance with slight changes. Shortly, forty SD rats (6 to 8 weeks, 200 to 220 g) applied in our study were gained from Nanjing University Model Animal Research Center (Nanjing, China), and they were subsequently cultivated from 20 to 25 ℃ and 45 percent of humidity, with free food and free water. All of the investigations were granted via Nanjing University Ethics Committee of the Nanjing University (Nanjing, China). These rats in the compound treatment and model groups were fed by high fat feed for the induction of the animal model of coronary artery atherosclerosis, the two compounds were subsequently applied through *ip* at 5 mg/ kg concentration. Eventually, the animal plasma could be harvested and the TNF-α level and IL-18 level was tested with indicated detection of enzyme-linked immunosorbent assay.

2.6. Real time reverse transcription-polymerase chain reaction (RT-PCR)

The real time reverse transcription-polymerase was implemented to detect the activation levels of the signaling pathway of NF-κb in the vascular endothelial cells after treating through the compound. This study was implemented fully adhere to the protocols' guidance with little changes. Generally, forty SD rats (between 6 and 8 weeks, from 200 to 220 g) utilized in our study were offered by Nanjing University Model Animal Research Center (Nanjing, China), and they were subsequently cultured from 20 to 25 ℃ and 45 percent of humidity, with a condition of free food and free water. All the experiment were authorized through Nanjing University Ethics Committee of the Nanjing University (Nanjing, China). These rats in the compound treatment and model groups were fed by high fat feed for the induction of the animal model of coronary artery atherosclerosis, the two compounds were subsequently employed through *ip* with 5 mg per kg concentration. After finishing this treatment, the animal vascular endothelial cells were collected, and the usage of TRIZOL was applied to conduct the extraction of the entire RNA in vascular endothelial cells. After testing its concentration, which was subsequently reverse trascripted into the cDNA via using indication kit. In the end, the *nf-κb* along with *p53* relative expression in vascular endothelial cells was detected, through utilizing the *gapdh* as an internal control. This study was conducted for 3 or more times, and the outcomes were described as mean ± SD.

Table 1 The complexes' architectural optimization along with their data of crystallography.

Sample	1	2
Formula	$C_{32}H_{36}Cd_2N_6O_{13}$	$C_{22}H_{24}CoN_3O_5$
Fw	937.49	469.37
Crystal system	triclinic	monoclinic
Space group	*P*-1	$P2_1/c$
a (Å)	8.649	12.2805(5)
b (Å)	10.1740(6)	13.1223(9)
c (Å)	11.6661(4)	13.2263(8)
α(°)	85.790(12)	90
β(°)	70.241(9)	95.069(5)
γ(°)	76.089(13)	90
Volume (Å^3)	937.74(10)	2123.1(2)
Z	1	4
Density (calculated)	1.660	1.4[illegible]
Abs. coeff. (mm^{-1})	1.204	0.84[illegible]
Total reflections	9010	90[illegible]
Unique reflections	3170	[illegible]231
Goodness of fit on F^2	1.00[illegible]	1.063
Final *R* indices [*I* greater than 2sigma(I^2)]	R_1 = 0.0331, wR_2 = 0.0[illegible]	R = 0.0770, wR_2 = 0.1637
R (all data)	R_1 = 0.0[illegible]49, wR_2 = 0.0968	R = 0.1320, wR_2 = 0.1784
CCDC	2,099,270	2,099,271

3. Results and discussion

3.1. Crystal structure of compound 1

The analysis of single crystal X-ray in crystallography reflected that in a triclinic space group of *P*-1, complex **1** was crystallizes, revealing a two-dimensional layered architecture, and its fundamental unit is composed of a Cd(II) ion, two halves L^{2-}, a 4-pybim, a terminal ligand of water together with one and a half lattice molecule of water. As displayed in the Fig. 1a, the Cd1 ion possesses a 6-coordinated octahedral structure, where the separation of Cd-O/N is between 2.224 (2) and 2.374(3) Å, this is defined via four carboxylic acid O atoms provided via three distinct L^{2-}, a N atom offered via a 4-pybim, and a terminal ligand of water. The dicarboxylic acid ligand of L^{2-} in compound **1** exhibit two diverse coordination patterns: where the first one mode with its two carboxylic acid groups in an uniform chelating pattern connecting two Cd(II) ions and the second other mode with its 2 carboxylic acid in an uniform monodentate pattern containing four Cd(II) ions. Two μ_2-carboxylic acid groups links 2 consecutive Cd(II) ions

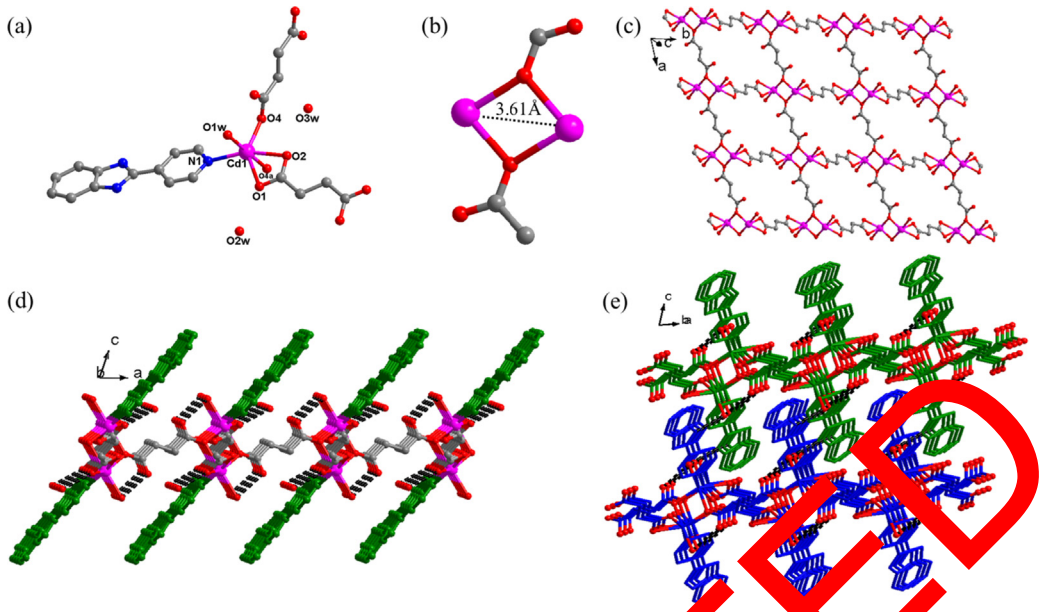

Fig. 1 (a) The Cd(II) ion coordination environment in the complex **1** (symmetry code a: 1-X, [illegible]). (b) The dinuclear subunit of $[Cd_2(COO)_2]$. (c) The two-dimensional Cd-L layer extending along plane *ab*. (c) The two-dimensional layered architecture of the compound **1**. (d) The complex **1**′s H-bonds linked three-dimensional supramolecular framework.

to create a dinuclear subunit of $[Cd_2(COO)_2]$, and the length of Cd···Cd distance is 3.61 Å (Fig. 1b). These dinuclear subunits $[Cd_2(COO)_2]$ are in-depth bridged through the L^{2-} to extend into a two-dimensional Cd-L^{2-} layer along plane *ab* (Fig. 1b). The 4-pybim molecules acting as a terminal ligands coordinated to Cd(II) ions with the benzimidazole spacers inclined upward and downward the 2D Cd-L^{2-} layer forming the final 2D layer of **1** (Fig. 1c). In this 2D layer, the H atoms from the lattice and coordinated molecules of water act as donors that can be accepted by carboxylate oxygen atoms, forming weak intramolecular O-H···O hydrogen bonds (OH...O = 2.684(5) and 2.763(13) Å, ∠OHO = 143.3° and 149.7°). Finally, the intermolecular hydrogen bonds of NH···O1w (NH...O1w = 2.779(5) Å and ∠NHO1w = 145.0°) between the NH– groups of benzimidazole spacers in one layer and the coordinated water molecules from the adjacent layer linked these two-dimensional layers into an interdigitated three-dimensional supramolecular framework (Fig. 1d).

3.2. Crystal structure of compound 2

The crystallographic study of X-ray suggested that the **2** also exhibits a two-dimensional layered architecture that comes from the space group $P2_1/c$ in monoclinic system. In the compound **2**′s fundamental unit, there exist a Co(II) ion, a cam^{2-}, a 4-pybim, as well as a free molecule of water. As exhibited in the Fig. 2a, the six-coordinated Co1 ion situated in the coordination structure of octahedron surrounded via five carboxylic acid O atoms belong to four diverse cam^{2-} and a N atom provided by a 4-pybim, and the spacing of Co-O/N in the range of 1.999(4)-2.356(4) Å. The carboxylic acid groups of cam^{2-} reveal two diverse coordination patterns, namely, bidentate chelating-bridging and bis-monodentate bridging patterns. As illustrated in the Fig. 2b, two symmetry-related Co(II) ions are connected through two bis-monodentate bridging carboxylic acid groups and two bidentate chelating-bridging carboxylic acid groups to provide a dinuclear subunit of $[Co_2(COO)_4]$ and the length of Co···Co is 2.92 Å. The above subunits are in-depth extended into a two-dimensional Co-cam layer with the linkage of the ligands cam^{2-} (Fig. 2c). Like **1**, the 4-pybim ligands also act as terminal ligands decorating up and down the 2D Co-cam layer, leading to the formation of the final 2D layer of **2** (Fig. 2d). The free molecules of water are glued to this two-dimensional layer *through* the intramolecular H-bonds of N-H...O1w and O1w-H...O3 (NH···O1w = 2.769(7) Å, O1wH1wa···O3 = 2.796(7) Å, ∠N2H2O1w = 167.9°, ∠O1Wh1waO3 = 169.5°). Viewing along crystallographic *c* axis, each 2D layer can be interdigitated by the benzimidazole spacers of 4-pybim ligands from the neighboring 2D layer directed through the weak interactions of Van der Waals, ultimately leading to the creation of interdigitated three-dimensional supramolecular framework (Fig. 2e).

3.3. Powder X-ray diffraction patterns (PXRD), thermogravimetric analyses (TGA) and FT-IR analysis

The compounds' polycrystalline samples were employed to perform the PXRD experiments under room temperature. The good consistencies of the experimental and simulated patterns demonstrate that the two compounds' massive products are pure phase. The differences in the intensity of the diffraction peaks may be resulted from the crystals preferred selection in the process of collecting the data (Fig S2).

To estimate the thermostablities of these two compounds, we also conducted TGA experiments using the powder samples of **1**–**2** under nitrogen atmosphere at the temperature of 30–800 ℃ (Fig. 3). The compound **1**′s curve of TGA suggests that its architecture occurs two-step weightlessness process: the first weightlessness appeared between 80 and 110 ℃ is owing to the

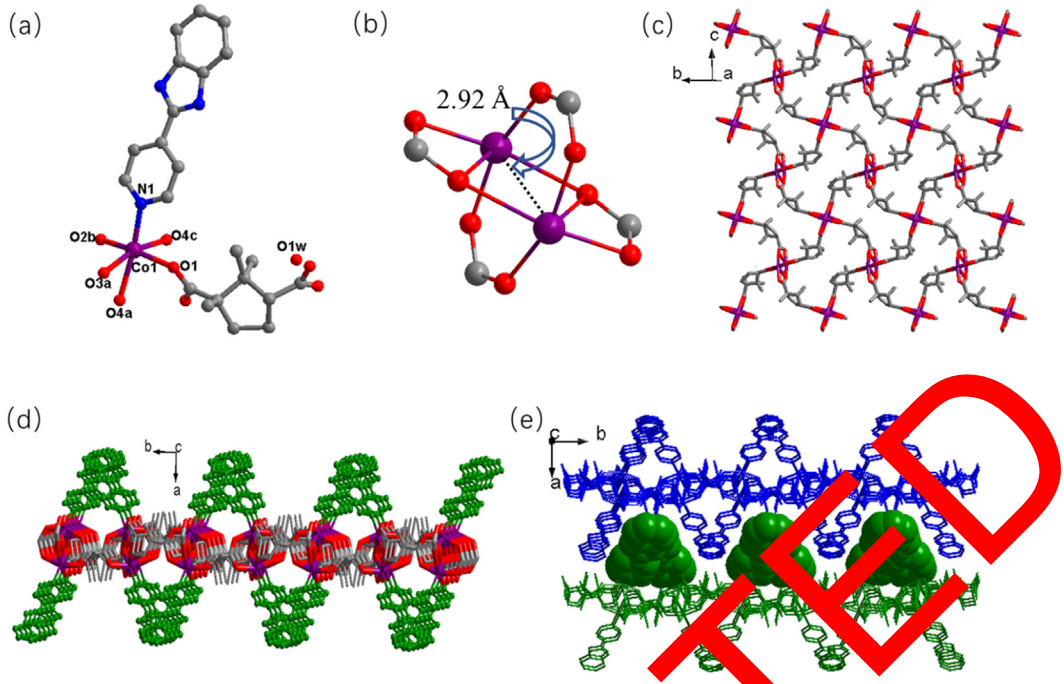

Fig. 2 (a) The Co(II) ion coordination environments in the complex **2** (symmetrical code a: 2-X,1/2 + Y,1/2-Z; b: 2-X, 1-Y, -Z; c: X, 1/2-Y, −1/2 + Z). (b) The dinuclear subunit of $[Co_2(COO)_4]$. (c) The compound **2**'s two-dimensional Co-cam layer. (d) The 2-dimensional layered structure of the complex **2**. (e) The interdigitated three-dimensional supramolecular framework directed through the weak interactions of Van der Waals.

release of the free and coordinated molecules of water (the calculated and observed value is 9.60% and 9.53%) and the second weightlessness appeared between 282 and 426 ℃ temperature was resulted from the organic ligand decomposition. And **2**'s curve of TGA reflects a two-step weightlessness process: the first weightlessness of 3.74% in the temperature of 76-96℃ is associated with the removal of lattice molecules of water, and the second one in the range of 285-4[illegible]℃ is also assigned to the combustion of the organic ligand. In the IR spectra of **1** and **2**, the absorption bands at 3462 and 3403 cm^{-1} for **1** and **2** can be assigned to the stretching vibration of hydroxyl (O–H) group, suggesting the presence of water molecules in the frameworks. The weak bands at [illegible]124 and 3114 cm^{-1} can be assigned to ν(Ar–H) of 4-pybim ligand. The band of **2** at 2931 cm^{-1} can be attributed to the ν(C–H) of methyl group in D-(+)-camphoric acid ligand. The characteristic bands of carboxyl groups in **1** are shown at 1555 cm^{-1} for asymmetric stretching and 1407 cm^{-1} for symmetric stretching, and those for **2** are shown at 1552 and 1403 cm^{-1}. The respective values of ($\nu_{asym}(COO^-)$-$\nu_{sym}(COO^-)$) (148 cm^{-1} for **1** and 149 cm^{-1} for **2**) suggest the presence of chelating coordination mode of the carboxylate groups in Pim^{2-}. The absence of the expected absorption bands at around 1700 cm^{-1} for the protonated carboxyl group indicates that all carboxyl groups of carboxylic acid ligands have been deprotonated. The bands at 1325 and 1288 cm^{-1} as well as

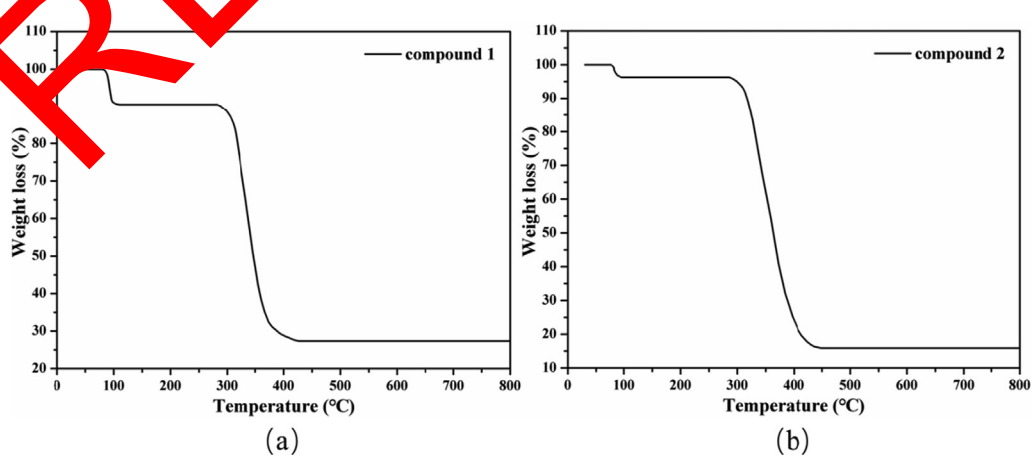

Fig. 3 The curves of TGA (a) for compound **1** and (b) for the **2**.

those from 1002 to 670 cm^{-1} in **1**, and the bands at 1342 and 1289 cm^{-1} as well as those from 1000 to 670 cm^{-1} in **2**, should be attributed to the imidazole of the 4-pybim ligands. These spectral information are consistent with the results of the single-crystal X-ray diffraction analyses.

3.4. Luminescent property of compound 1

Considering the large π-electron conjugated system of 4-pybim ligand, herein, the solid-stated luminescent spectra of **1** as well as 4-pybim ligand were measured at room temperature (Fig. 4). With 350 nm excitation, the free ligand of 4-pybim exhibits a strong emission band, and at 396 nm, the maximum peak is appeared, owing to the $\pi^* \rightarrow \pi$ electron transition of π-conjugated system of 4-pybim ligand (Zhang et al., 2020). Under the same excitation wavelength, the luminescent spectrum of **1** shows 23 nm red-shift in contrast to that of free ligand 4-pybim, and the complex **1**′s maximum emission peak occurs at around 419 nm. Due to the electronic configuration of d^{10} of Cd(II) ion, the **1**′s luminescence is neither MLCT nor LMCT, it principally stem from the transition of $\pi^* \rightarrow \pi$ of 4-pybim in the ligand. The red-shift of the emission of **1** compared with that of the 4-pybim ligand should be due to the coordination of the ligand with the metal center, which could change the ligand geometry and enhance the strength of rigidity in the solid state (Qin et al., 2011).

3.5. Optical band gap and photocatalytic property of compound 2

The optical band gap of Eg, an important indicator to evaluate the semiconductor property of **2**, was calculated by the function of Kubelka–Munk exploiting the data of ultraviolet–visible diffuse reflectance (Fig S3) (Qian et al., 2019; Wang et al., 2019; Qian et al., 2021). As displayed in Fig. 5a, the band **2**′s band-gap is 3.30 eV, indicating that compound **2** can acts as a potential UV photoactive material. Its photocatalytic performance was further accessed by the methyl violet photodegradation under an irradiation of ultraviolet light. At 580 nm, the maximum MV absorption peak was selected to monitor the process of photocatalysis. As reflected in the Fig. 5b, employing **2** as the photocatalyst, the absorption intensities of 580 nm for MV decrease gradually as the time extension of UV light irradiation. The comparative test in absence of **2** was also conducted at the same conditions. As shown in Fig. 5c, without the photocatalyst of **2**, the degradation efficiency of MV is calculated to be 18.1% after 105 min of UV light irradiation. While, in the presence of **2**, the degradation efficiency of MV increased to 83.4% after the 140 min irradiation, demonstrating that **2** is very efficient for the MV photocatalytic degradation under ultraviolet light. After the reaction of photocatalysis, its PXRD pattern match well with that of the as-synthesized sample, indicating that the structure of **2** was not damaged during the photodegradation process (Fig. S1b). As shown in Fig. 5d, it is obvious that the MV degradation reaction adhere to the first-order kinetic equation, that is $\ln(C_t/C_0) = -kt + b$, and the degradation rate constant of k is 0.01435 min^{-1}. As far as we know, the photocatalytic activity of this compound is better than that of formerly reported compounds under the similar catalytic conditions such as $[Zn_2(pa)_2(bip)_2]$, [Cd(L)(Hbpz)] and [Cu(bidpe)(mpa)

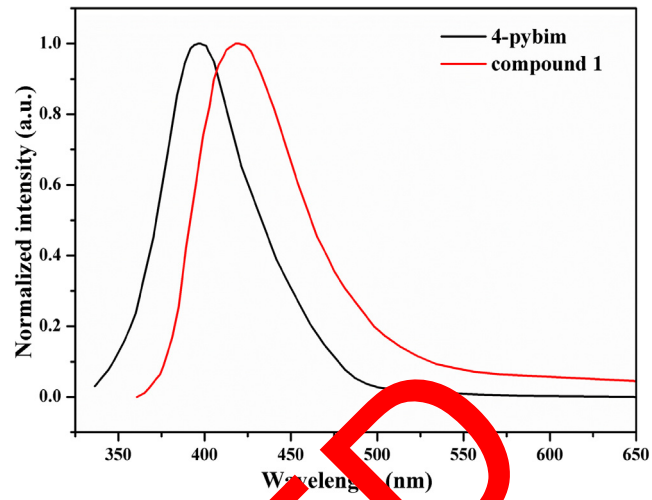

Fig. 4 The emission spectra of free ligand 4-pybim and complex **1** at environment temperature.

(H_2O)], which needs more reaction time and have less catalytic efficiency (Wang et al., 2019; Cai et al., 2019; Zong et al., 2019). The divergences between the photocatalytic activities in these CPs may be arising due to the differences in their framework because of the variation in the nature of *N*-donor ancillary ligands and the conjugated systems in the carboxylate ligands which affect the electronic communications within the frameworks.

From the results of photo-degradation, the catalytic mechanism is worth studying. A series of factors may affect CPs degradation ability, such as the coordination environments of the central metals, the specific surface area, the structures of CPs, and the optical band gap. It is known that when CPs are exposed to UV light (photo-excitation), the electrons transfer from the highest occupied molecular orbital (HOMO) contributed by the oxygen and/or nitrogen 2p bonding orbital (valence band) to the lowest unoccupied molecular orbital (LUMO) contributed by an empty metal orbital (conduction band). The hydroxyl radical ·OH, being a very strong oxidizing agent, can oxidize most of the dyes to the mineral end-products. The hydroxyl radical trapping experiments were carried out to detect the main oxidative species in the photocatalytic process to conform the catalytic mechanism using isopropanol (IPA), ammonium oxalate (AO), and benzoquinone (BQ) as scavengers. As shown in Fig. S5, when 1 mM IPA as a radical scavenger was added into the reaction solution with the existence of **2**, the photo-degradation efficiency of dyes is significantly inhibited for MV [decreased from 83.4% to 40.5%] under UV light irradiation. The results indicate that ·OH radicals were the main active species in the photocatalytic reaction process.

3.6. Compound could significantly reduce the releasing of inflammatory cytokines into the plasma

In the creation of coronary artery atherosclerosis, there was commonly combined with the enhanced inflammatory cytokines level in plasma. Thus, after the synthesis of the new compounds, their biological activity was firstly evaluated with ELISA assay by measuring the inflammatory cytokines in

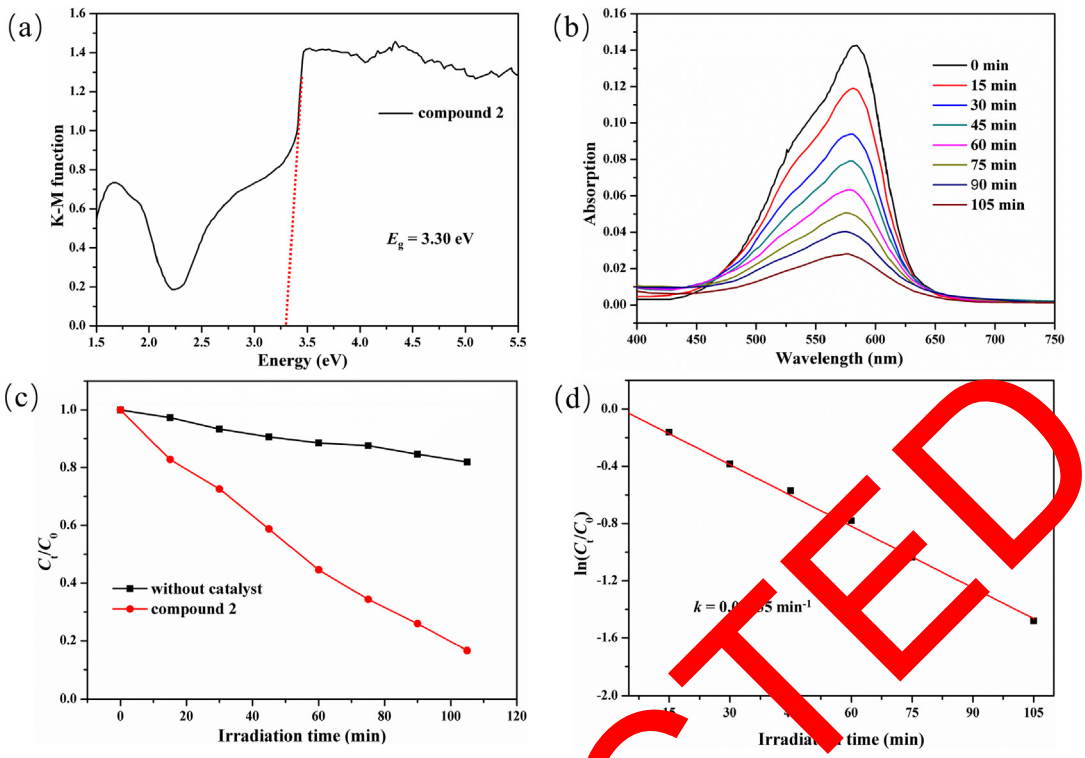

Fig. 5 (a) The diffuse reflectance spectrum for the function of Kubelka-Munk versus energy for compound **2**. (b) The ultraviolet–visible absorption spectra of MV in the existence of **2**. (b) The plots of degradation efficiencies of MV with or without **2** as photocatalyst. (c) The plots of C/C_0 vs. the time of irradiation. (d) The first-kinetic plot for the MV photodegradation in the existence of photocatalysts.

the plasma. As the data displayed in the Fig. 6, we observe that model group exhibits a remarkably increased inflammatory cytokines level than control group. After treating via the **1**, the inflammatory cytokines levels of model group were evidently decreased. Nevertheless, compound **2** exhibited only slight effect against the inflammatory cytokines levels in plasma.

3.7. Compound obviously inhibited the activation levels of NF-κb signaling pathway in the vascular endothelial cells

In this study, we have proven that the **1** reflects superior application values against the treatment of coronary artery atherosclerosis via decreasing the TNF-α level and IL-18 level

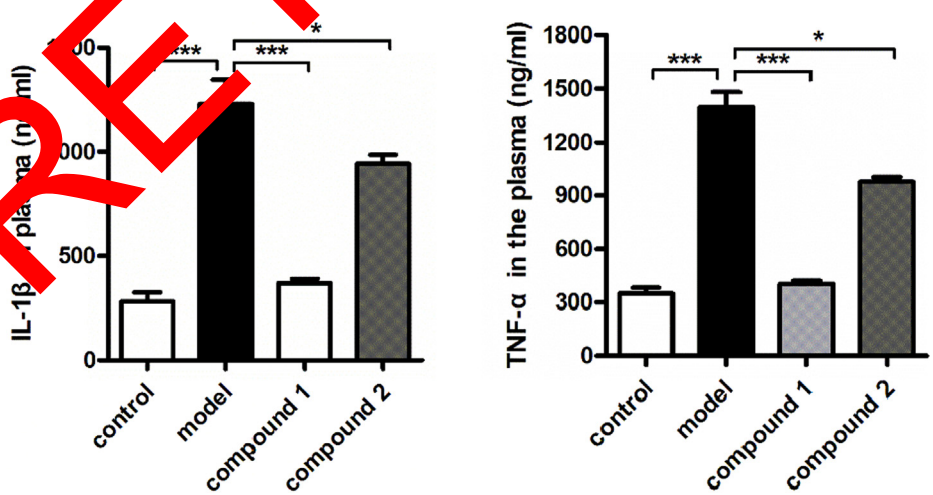

Fig. 6 Remarkably decreased inflammatory cytokines releasing levels in plasma after treating via compound. The animal model of coronary artery atherosclerosis was generated and then the injection of compounds was conducted by *ip* at 5 mg per kg concentration. The animal plasma could be harvested and the suggested enzyme-linked immunosorbent assay detection assay was exploited to test the TNF-α level and IL-18 level released by the vascular endothelial cells into plasma.

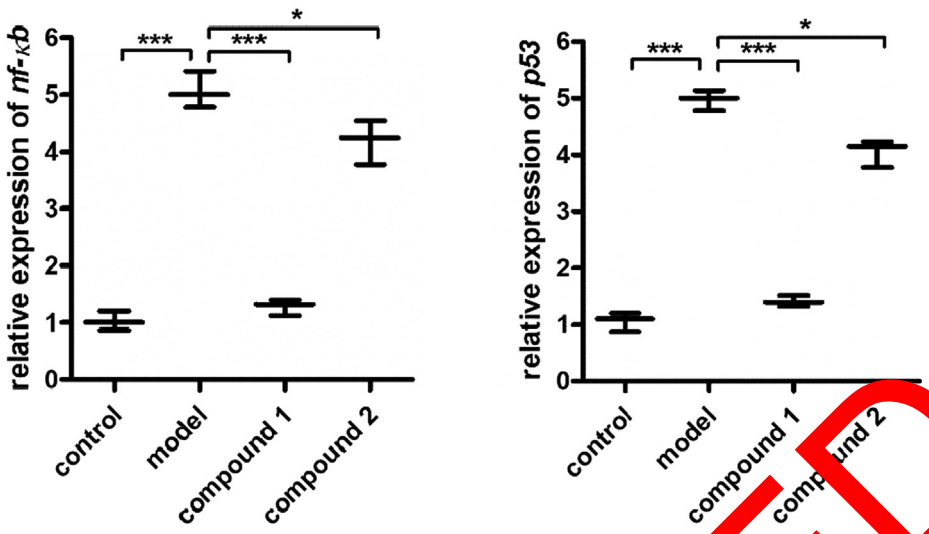

Fig. 7 Evidently inhibited activation levels of signaling pathway of NF-κb in vascular endothelial cells after treating by compound. The coronary artery atherosclerosis was generated and then the injection of compounds was conducted by *ip* at 5 mg per kg concentration. The vascular endothelial cells were separated and the signaling pathway activation of NF-κb in vascular endothelial cells was tested via exploiting real time RT-PCR.

released through vascular endothelial cells into the plasma. As the signaling pathway of NF-κb in the vascular endothelial cells regulated the TNF-α releasing and IL-18 releasing, therefore, the real time reverse transcription-polymerase was in-depth accomplished to detect the activation levels of the signaling pathway of NF-κb in the vascular endothelial cells. The data in the Fig. 7 indicates that the model group exhibits evidently higher activation levels of the signaling pathway of NF-κb than control group. After the complex **1** treatment, the activation levels of the signaling pathway of NF-κb was significantly inhibited. Different from compound **1**, the inhibition of compound **2** on the signaling pathway of NF-κb was much weaker.

4. Conclusions

In summary, we have successfully prepared two new coordination polymers via using the mixed-ligand method. As functional materials, compound **1** emits intense 4-pybim ligand-centered luminescence, and compound **2** possesses superior photocatalytic performance for the MV photodegradation under ultraviolet light. The ELISA assay data exhibited that the **1** could obviously down-regulated the inflammatory cytokines levels released into plasma after carrying out treatment than the compound **2**. Besides, the activation of the signaling pathway of NF-κb in vascular endothelial cells was obviously inhibited through the **1**, but not the **2**. Ultimately, we can find that the **1** was more superior to complex **2** against the treatment of coronary artery atherosclerosis via inhibiting the signaling pathway of NF-κb in vascular endothelial cells.

Data Availability

Selected bond lengths (Å) and angles (°) for compounds **1**–**2** (Table S1), The IR spectra of complexes **1**–**2** (Fig. S1), The PXRD patterns (a) for compound **1** and (b) for compound **2** (Fig. S2), The UV–Vis spectrum for **1** recorded in solid state (Fig. S3), View of the adsorbent **1** on MV in dark (Fig. S4), Change in the catalytic efficiency in the presence of **2** and different active species as scavengers (Fig. S5), the information could be found in the supporting information file.

Declaration of Competing Interest

The authors declare that they have no known competing financial interests or personal relationships that could have appeared to influence the work reported in this paper.

Acknowledgments

The research was supported by the National Natural Science Foundation of China (81770426) and Open subject of the key laboratory of Myocardial Ischemia of Ministry of Education (KF202116).

Appendix A. Supplementary material

Supplementary data to this article can be found online at https://doi.org/10.1016/j.arabjc.2021.103498.

References

Banerjee, D., Hu, Z., Li, J., 2014. Luminescent metal–organic frameworks as explosive sensors. Dalt. Trans. 43, 10668–10685.

Boudoulas, K.D., Triposciadis, F., Geleris, P., Boudoulas, H., 2016. Coronary Atherosclerosis: Pathophysiologic Basis for Diagnosis and Management. Prog. Cardiovasc Dis. 58, 676–692.

Cai, S.L., Lu, L., Wu, W.P., Wang, J., Sun, Y.C., Ma, A.Q., Singh, A., Kumar, A., 2019. A new mixed ligand based Cd(II) 2D coordination polymer with functional sites: Photoluminescence and photocatalytic properties. Inorg. Chim. Acta 484, 291–296.

Cassemiro, B.G., Santos, J.S., Oliveira, W.X.C., Pereira-Maia, E.C., Galvão, B.R.L., Pim, W.D., Silva-Caldeira, P.P., 2020. Dinuclear copper(II) complex with a benzimidazole derivative: Crystal

structure, theoretical calculations, and cytotoxic activity. Appl. Organomet. Chem. 34, e4550.

Dutta, A., Pan, Y., Liu, J.Q., Kumar, A., 2021. Multicomponent isoreticular metal-organic frameworks: Principles, current status and challenges. Coord. Chem. Rev. 445, 214074.

Fan, L., Zhao, D., Li, B., Chen, X., Wang, F., Deng, Y., Niu, Y., Zhang, X., 2021. An exceptionally stable luminescent cadmium(ii) metal–organic framework as a dual-functional chemosensor for detecting Cr(vi) anions and nitro-containing antibiotics in aqueous media. CrystEngComm 23, 1218–1225.

Fan, L., Zhao, D., Li, B., Wang, F., Deng, Y., Peng, Y., Wang, X., Zhang, X., 2022. Luminescent binuclear Zinc(II) organic framework as bifunctional water-stable chemosensor for efficient detection of antibiotics and Cr(VI) anions in water. Spectrochim. Acta Part A Mol. Biomol. Spectrosc. 264, 120232.

He, H., Hashemi, L., Hu, M.L., Morsali, A., 2018. The role of the counter-ion in metal-organic frameworks' chemistry and applications. Coord. Chem. Rev. 376, 319–347.

Hu, M.L., Safarifard, V., Doustkhah, E., Rostamnia, S., Morsali, A., Nouruzi, N., Beheshti, S., Akhbari, K., 2018. Taking organic reactions over metal-organic frameworks as heterogeneous catalysis. Micropor. Mesopor. Mat. 256, 111–127.

Hu, M.L., Razavi, S.A.A., Piroozzadeh, M., Morsali, A., 2020. Sensing organic analytes by metal–organic frameworks: a new way of considering the topic. Inorg. Chem. Front. 7, 1598–1632.

Libby, P., Theroux, P., 2005. Pathophysiology of coronary artery disease. Circulation 111, 3481–3488.

Liu, J.Q., Luo, Z.D., Pan, Y., Singh, A.K., Trivedi, M., Kumar, A., 2020. Recent developments in luminescent coordination polymers: Designing strategies, sensing application and theoretical evidences. Coord. Chem. Rev. 406, 213145.

Liu, W., Pan, Y., Zhong, Y., Li, B., Ding, Q., Xu, H., Qiu, Y., Ren, F., Li, B., Muddassir, M., Liu, J.Q., 2021. A multifunctional amine UiO-67 metal-organic framework for enhancing antitumor cytotoxicity through bimodal drug delivery. Chem. Eng. J. 412, 12789[illegible].

Pan, Y., Luo, Z.D., Wang, X., Chen, Q., Chen, J., Guan, Y., Liu, D., Xu, H., Liu, J.Q., 2020. A versatile and multifunctional metal–organic framework nanocomposite toward chemo-photodynamic therapy. Dalt. Trans. 49, 5291–5301.

Qian, Y., Du, J., Kang, D.J., 2019. Enhanced electrochemical performance of porous Co-doped TiO_2 nanomaterials prepared by a solvothermal method. Micropor. Mesopor. Mat. 273, 148–155.

Qian, Y., Wang, L., Du, J., Yang, H., Li, M., Wang, Y., Kang, D.J., 2021. A High Catalytic Activity Photocatalyst Based on Porous Metal Sulfides/TiO_2 Heterostructures. Adv. Mater. Inter. 8, 2001627.

Qin, L., Hu, J.S., Li, Y.Z., Zheng, H.G., 2012. Three New Coordination Polymers Based on One Reduced Symmetry Tripodal Linker. Cryst. Growth Des. 11, 115[illegible]121.

Qin, J.H., Zhang, H., Sun, P., Huang, Y.D., Shen, Q., Yang, X.G., Ma, L.F., 2020. Induced highly dense assembly of porphyrin in MOF nanosheets for photodynamic therapy. Dalt. Trans. 49, 17772–17778.

Sabithakala, T., Chittireddy, V.R.R., 2018. DNA binding and in vitro anticancer activity of 2-((1H -benzimidazol-2-yl)methylamino) acetic acid and its copper(II) mixed-polypyridyl complexes: Synthesis and crystal structure. Appl. Organomet. Chem. 32, e4550.

Sheldrick, G.M., 2015. Crystal structure refinement with SHELXL. Acta Crystallogr. Sect. C: Struct. Chem. 71, 3–8.

Singh, A., Singh, A.K., Liu, J.Q., Kumar, A., 2021. Syntheses, design strategies, and photocatalytic charge dynamics of metal–organic frameworks (MOFs): a catalyzed photo-degradation approach towards organic dyes. Catal. Sci. Technol. 11, 3946–3989.

Wang, J., Lu, L., He, J.R., Wu, W.P., Gong, C., Fang, L., Pan, Y., Singh, A.K., Kumar, A., 2019. Photocatalytic performances of two new Cd(II) and Zn(II)-based coordination polymers. J. Mol. Struct. 1182, 79–86.

Wang, F., Tian, F., Deng, Y., Yang, [illegible], Zhang, H., Zhao, D., Li, B., Zhang, X., Fan, L., 2021. Cluster Based Multifunctional Copper (II) Organic Framework as a Photocatalyst in the Degradation of Organic Dye and as an Electrocatalyst for Overall Water Splitting. Cryst. Growth Des. 21, 4242–4249.

Wang, Y., Zhang, F., Yang, M., Wang, Z., Ren, Y., Cui, J., Zhao, Y., Du, J., Li, K., Wang, W., Wang, D.J., 2019. Synthesis of porous MoS_2/CdSe/TiO_2 photoanodes for photoelectrochemical water splitting. Micropor. Mesopor. Mat. 284, 403–409.

Wen, G.X., Yan, M., Wu, X.Q., Wu, Y.P., Dong, W.W., Zhao, J., Li, D.S., Ma, L.F., 2016. A multi-responsive luminescent sensor based on a super-stable sandwich-type terbium(iii)–organic framework. Dalt. Trans. 45, 15492–15499.

Wu, X.X., Fu, [illegible]R., Han, M.L., Zhou, Z., Ma, L.F., 2017. Tetraphenylethylene Immobilized Metal-Organic Frameworks: Highly Sensitive Fluorescent Sensor for the Detection of $Cr_2O_7^{2-}$ and Nitroaromatic Explosives. Cryst. Growth Des. 17, 6041–6048.

[illegible], J.J., Bigdeli, F., Liu, J.P., Hu, M.L., Morsali, A., 2018. Organic-assisted synthesis and DNA interaction studies of two new Ru complexes; RuO_2 nanoparticles preparation. Nanomedicine 13, 2691–2708.

Zhang, D., Bi, C., Zong, Z., Fan, Y., 2020. Three different Co(II) metal–organic frameworks based on 4,4' bis(imidazolyl)diphenyl ether: syntheses, crystal structure and photocatalytic properties. J. Inorg. Organomet. P. 30, 5148-5156.

Zhao, D., Song, J., Zhang, X., Wang, F., Li, B., Yang, L., Deng, Y., Li, Q., Fan, L., 2021. A Pillar-layered Binuclear 3D Cobalt(II) Coordination Polymer as Electrocatalyst for Overall Water Splitting and Chemosensor for Cr(VI) Anions Detection. CrystEngComm. https://doi.org/10.1039/D1CE00.

Zong, Z., Fan, C., Bi, C., Zhang, X., Luo, R., Meng, X., Jin, F., Fan, Y., 2019. Highly selective functional luminescent sensor toward Cr (VI)/Fe(III) ion and nitrobenzene based on metal–organic frameworks: Synthesis, structures, and properties. J. Solid State Chem. 270, 651–665.